[1] The origin of water-vapor rings in tropical cold pools

Wolfgang Langhans[1] and David M. Romps[1,2]

Corresponding author: W. Langhans, Earth Sciences Division, Lawrence Berkeley National Laboratory, Mailstop 74R316C, Berkeley, CA 94720, USA. (wlanghans@lbl.gov)

[1]Earth Sciences Division, Lawrence

Berkeley National Laboratory, Berkeley,

California, USA.

[2]Department of Earth and Planetary

Science, University of California, Berkeley,

California, USA.

Tropical deep convection over the ocean is found to grow preferentially from thermodynamically pre-conditioned regions of high specific humidity and, thus, high moist static energy. For this reason, rings of enhanced specific humidity at the leading edges of evaporatively driven cold pools have recently received considerable attention. The prevailing theory explains these rings by the water-vapor source from the evaporation of rain drops below cloud base. Their origin is studied in this letter using large-eddy simulations of individual cumulus clouds that rise into a tropical atmosphere over ocean. It is demonstrated that – in contrast to this theory – water-vapor rings are primarily explained by surface latent-heat fluxes rather than by the evaporation of rain. This finding implies that conceptual models used in subgrid-scale parameterizations of deep convection should consider the formation of rings of increased specific humidity by the cold-pool-induced enhancement of surface fluxes.

1. Introduction

The presence of cold pools within the planetary boundary layer (PBL) over tropical oceans is crucial for the interaction between the PBL and the free troposphere through their impact on deep convection. The modulation of deep convection by cold-pool dynamics has commonly been hypothesized to result from two processes: a) the mechanical lifting of ambient air at the leading edge of cold pools as known from squall line dynamics [e.g., *Moncrieff and Liu*, 1999; *Droegemeier and Wilhelmson*, 1985; *Rotunno et al.*, 1988] and b) the preconditioning of the boundary layer for deep convection through cold-pool induced enhancement of the moist static energy inside the PBL [*Tompkins*, 2001a, b, the latter will be referred to as TO1].

The latter thermodynamic argument is based on the observation that cold pools exhibit rings of enhanced water-vapor content and thus high moist static energy within their leading edges. These rings of enhanced water-vapor content are visible from horizontal distributions of near-surface water-vapor mixing ratios. They have been observed in gust fronts over tropical oceans [*Addis et al.*, 1984] and have been described in various cloud-resolving and large-eddy simulations of deep tropical convection and precipitating trade-wind cumuli (e.g., TO1; *Xue et al.* [2008]; *Khairoutdinov et al.* [2009]; *Moeng et al.* [2009]; *Moeng and Arakawa* [2012]; *Seifert and Heus* [2013]; *Torri et al.* [2015]).

Even if convective updrafts do not originate from preconditioned air inside an active cold pool (as argued by TO1), the positive moisture anomaly carried near the edges of recovering cold pools will later favor the triggering upon collision with a more active (i.e., younger) cold pool. This is described in TO1, who found that convection grows from

PBLs with a pre-existing vapor anomaly of about $+1$ g kg^{-1}. The observed vapor rings are of relevance also as they may eventually cluster to larger moist patches [*Schlemmer and Hohenegger*, 2014] and trigger relatively wide – thus less entraining and deeper – clouds [*Boing et al.*, 2012]. Several other studies demonstrated that deep convective updrafts over tropical oceans preferentially grow from anomalously moist boundary layers [*Kingsmill and Houze*, 1999; *Seifert and Heus*, 2013; *Li et al.*, 2014; *Torri et al.*, 2015]. Understanding the mechanisms behind the formation of these vapor rings is thus critical to understanding the influence of cold pools on deep convection. Although some convection parameterizations in GCMs account for the mechanical lifting by cold pools [*Qian et al.*, 1998; *Grandpeix and Lafore*, 2010; *Rio et al.*, 2013], air is generally modeled as being lifted from the unperturbed (i.e., environmental) part of the boundary layer without accounting for the effects of these vapor rings.

Moreover, despite the agreement on the relevance of these moist anomalies, different explanations were proposed for the origin of these rings. The prevailing hypothesis proposed by TO1 is that these rings form due to the evaporation of raindrops within the sub-cloud layer before the downdraft reaches the PBL. In line with TO1, *Seifert and Heus* [2013] argue that evaporation of rain is key to the existence of these vapor rings. In contrast, *Li et al.* [2014] argue that evaporation of rain does not contribute to the anomalous moisture. To seed even more confusion, *Li et al.* [2014] and *Schlemmer and Hohenegger* [2014] conclude that, in contrast to TO1, the enhanced vapor content is found *outside* of cold pools. This underlines the incongruity of previous explanations. On top of that, the role of surface latent-heat fluxes remains unclear.

In this paper we seek a physical explanation of the origin of these vapor rings. More specifically, we seek to answer the following questions:

1. What is the origin of water-vapor rings in tropical cold pools?

2. What are the individual contributions from evaporation of rain, surface latent-heat fluxes, and the existing (i.e., pre-rain) PBL moisture anomaly?

3. Are the underlying physics in line with the conceptual ideas proposed by TO1?

To address these questions, we carry out large-eddy simulations and study the vapor sources using passive and active tracers of water-vapor mass (see section 2). The simulations are motivated by atmospheric conditions commonly observed in radiative-convective equilibrium (RCE) over tropical oceans.

2. Numerical setup

2.1. General description

Numerical simulations are carried out using Das Atmosphärische Modell [DAM, *Romps*, 2008]. DAM solves the compressible equations in flux form using a split-explicit [*Klemp et al.*, 2007] total-variation-diminishing (TVD) 3rd-order Runge-Kutta (RK3) discretization in time [*Shu and Osher*, 1988]. Advection is discretized using a 3rd-order upstream scheme and a positive-definite flux limiter [*Thuburn*, 1996] is applied to the moisture scalars. Following the concept of implicit LES [e.g., *Margolin et al.*, 2006], no subgrid-scale (SGS) turbulence closure is applied. The lateral boundary conditions are cyclic.

A no-slip bottom boundary condition is applied and surface drag and sensible and latent-heat fluxes are parameterized by bulk transfer laws using a drag/transfer coefficient of $C_D = 1.5 \times 10^{-3}$. For example, the surface moisture flux is parameterized as

$\rho\overline{q_v'w'}|_{\mathrm{s}} = -C_D|\mathbf{u}|_1(q_v|_1 - q_v^*|_{\mathrm{sst}})$ with $q_v^*|_{\mathrm{sst}}$ the saturation specific humidity for a sea sur-
face temperature (SST) of 300 K and with index 1 denoting variables on the first model
level.

The microphysical mass exchange rates among six water classes are parameterized using
the Lin-Lord-Krueger one-moment bulk scheme [*Lin et al.*, 1983; *Lord et al.*, 1984; *Krueger
et al.*, 1995] with minor adaptions as described by *Langhans et al.* [2015]. The bulk
formulation distinguishes between six water classes: water vapor, cloud liquid water,
cloud ice, rain, snow, and graupel.

2.2. Simulations

Single cumulus clouds are simulated in this study similar to the ones investigated by
Langhans et al. [2015]. Clouds are forced from an initially axisymmetric "bubble" pertur-
bation in the center of the numerical domain. The advantage of this configuration is that
the emerging cold pool remains quasi-axisymmetric without any collisions with other cold
pools as it would be in simulations of RCE. Motivated by cold pools commonly observed
in RCE, the initialized background temperature and specific humidity profiles $T_0(z)$ and
$q_{v0}(z)$ are taken from previously conducted RCE runs over an SST of 300 K [see *Romps
and Kuang*, 2011, section 3].

We focus on simulating the period of cold-pool initiation and propagation. The domain
and grid setup are thus tailored to achieve high resolution inside the boundary layer with
a relatively coarse and inexpensive resolution above. The dimensions of the numerical
domain are $(L_x, L_y, L_z) = (20, 20, 14.1)$ km. A five-layer structure is used to distribute
levels in the vertical. Three sections with constant grid spacings δz of 10, 190, and 610

m, respectively, are separated by two sections that allow for smooth transitions based on tanh functions. The interfaces between the layers are located at 400, 3400, 5300, and 9300 m. The lowermost layer with $\delta z = 10$ m fully includes the emerging cold pools. The horizontal grid spacing is 50 m.

Two simulations are presented in this letter: R1 and R2. Moist convection in R1 is initiated from an anomalously warm and moist boundary layer that exhibits a $q'_{v0} = 1$ g kg^{-1} perturbation with a horizontal scale of about 3 km. This moisture anomaly is thought to represent the moisture excess caused by an older cold pool and the chosen scale and magnitude is in line with findings in TO1 (his Fig. 7) and others (see introduction). The sensitivity to this initialized moisture perturbation is tested in run R2 which starts without this moisture perturbation.

To kick off convection, a small-scale temperature perturbation of magnitude $\delta T = 1$ K is prescribed in both R1 and R2, as

$$T(r, z) = T_0(z) + (\delta T + \zeta) \exp\left[-(r/r_b)^2 - (z/z_b)^2\right], \tag{1}$$

with $r = \sqrt{x^2 + y^2}$, height z, $r_b = 1000$ m, $z_b = 500$ m, and random perturbations $\zeta \in [-0.05, 0.05]$. In case of R1, the q_v perturbation is added as

$$q_v(r, z) = q_{v0}(z) + q'_{v0} \exp\left[-(r/R_b)^2 - (z/Z_b)^2\right], \tag{2}$$

with $q'_{v0} = 10^{-3}$ g g^{-1}, $R_b = 3000$ m, and $Z_b = 500$ m. Simulations are carried out for two hours to capture the full life cycle of the cloud, including the dissipating stage and – most importantly – cold-pool propagation.

2.3. Water-vapor tracers

The individual contributions to the ring-shaped water-vapor mass anomaly are identified here by advancing tracers of water-vapor mass of different origin. To do so, tracer mass fractions are initialized at time $t_i = 1040$ s, which is right before rain starts falling into the sub-cloud layer (i.e., pre-rain). A first (passive) tracer mass fraction q'_{pbl} represents the pre-rain PBL perturbation existing at time t_i. To define this perturbation, the water-vapor field at time t_i is decomposed into a base state q_{base} and a perturbation q'_{pbl}. The former is horizontally uniform inside the sub-cloud layer and defined as

$$q_{\mathrm{base}}(x, y, z, t_i) = \gamma(z) q_v(x, y, z, t_i)$$

$$+ \left[1 - \gamma(z)\right] q_v^\infty(z) \tag{3}$$

$$\gamma(z) = 0.5 + 0.5 \tanh\left[0.02(z - 500)\right], \tag{4}$$

with $q_v^\infty(z) = q_v(-L_x/2, -L_y/2, z, t_i)$ the specific humidity profile in a corner of the domain. The perturbation q'_{pbl} is defined as $q'_{\mathrm{pbl}} = q_v - q_{\mathrm{base}}$. Function $\gamma(z)$ goes from 0 to 1 across the cloud base at 500 m, such that q_{base} is horizontally uniform below cloud base and $q_{\mathrm{base}} = q_v$ and $q'_{\mathrm{pbl}} = 0$ above cloud base at time t_i. The base-state mass fraction q_{base} forms the second passive tracer to be advanced. Moreover, two active tracer mass fractions q'_{lh} and q'_{er} are advanced to study the water-vapor mass due to surface latent-heat fluxes and due to evaporation of rain, respectively. Both are initialized to zero at time t_i.

The mass M_χ of each tracer χ is advanced as

$$\frac{\partial(q_\chi \rho)}{\partial t} = -\frac{\partial(q_\chi \rho \mathbf{u})}{\partial \mathbf{x}} + S_\chi, \tag{5}$$

with tracer mass fraction $q_\chi = M_\chi/(M_a + M_v + M_l + M_s)$, density ρ, mass of dry air M_a, water vapor M_v, liquid water M_l, and solid water M_s, and tracer mass source S_χ. The source term is zero for the two passive tracers q_{base} and q'_{pbl}. The sources of the active

131 tracers q'_{lh} and q'_{er} are the surface moisture flux convergence $S_{lh} = -\partial_z \rho \overline{q'_v w'}|_s$ and the

132 evaporation of rain $S_{er} = \rho E$, respectively.

133   We find that, at any time, the sum of q_{base}, q'_{pbl}, q'_{lh}, and q'_{er} is almost identical to q_v. The

134 difference is significantly smaller than the water-vapor perturbations we are interested in,

135 confirming that surface latent-heat fluxes and evaporation of rain are the only sources of

136 relevance to the water-vapor budget of cold pools in our simulations.

3. The origin of water-vapor rings

3.1. Horizontal distributions

Our simulations reveal considerable agreement with the observations from previous

simulations of tropical convection (e.g., TO1; *Moeng et al.* [2009]; *Torri et al.* [2015]).

Distinct water-vapor rings appear near the edge of radially spreading cold pools with

specific humidities about 0.6 to 1.0 g kg^{-1} higher than in the unperturbed PBL away

from the cold pool. To illustrate this and to identify the origin of these rings, we show

density-weighted vapor mass fractions for the lowest 100 meters, defined as

$$\overline{q'}_v = \frac{\int_0^{100m} dz' \rho(z') q'_v(z')}{\int_0^{100m} dz' \rho(z')}, \tag{6}$$

137 with $q'_v(x, y, z) = q_v(x, y, z) - q_v^{\infty}(z)$ a perturbation with respect to the far-field envi-

138 ronment a time t_i. Analogously, average mass fractions are computed for the base-state

139 perturbation $q'_{base} = q_{base} - q_v^{\infty}$, for the pre-rain PBL perturbation q'_{pbl}, for the latent-heat

140 flux perturbation q'_{lh}, and for the perturbation q'_{er} due to evaporation. The evolution of

141 these average mass fractions is illustrated for R1 in Fig. 1 by showing snapshots after

142 26, 62, and 98 minutes. To very good approximation, the actual perturbation of the

143 vapor mass fraction shown in the first column results from the sum of the individual

144 perturbations shown in the other columns.

145   During the early stage, at $t = 26$ min, the water-vapor ring consists mostly of water-

146 vapor mass that existed already in the PBL before the onset of rainfall. The pre-rain

147 PBL water-vapor mass gets displaced laterally by the approaching dry air from aloft. At

148 that time, the contributions from latent-heat fluxes and from evaporation of rain are very

149 small (≤ 0.2 g kg^{-1}) inside regions with anomalously high vapor contents. The water-

150 vapor mass originating from rain peaks inside the cold pool and is collocated with the

151 negative perturbation due to the downward advection of the base state.

152   The vapor perturbation from surface fluxes grows rapidly in time and, by $t = 62$ min,

153 has reached peak magnitudes larger than those due to the pre-rain PBL anomaly. Then,

154 only the water-vapor mass from surface fluxes causes a distinct narrow ring-like anomaly.

155 The largest mass fractions from evaporated rain are carried in the dry air mass that sunk

156 down from aloft. The water-vapor mass from evaporation thus peaks in the dry center

157 of the cold pool with a relatively homogeneous mass distribution towards the outer edge.

158 The pre-rain PBL perturbation gets dispersed radially outwards in time leading to an

159 increasing areal coverage and to decreasing peak perturbations.

3.2. Vertical distributions

160   To better understand the transport and origin of water-vapor mass inside the cold pool,

161 we analyze the average vertical distribution of water-vapor density and its individual

162 contributions in a next step. We first identify the radius at the leading edge of the cold-

163 pool $R(\varphi)$ for each azimuth angle φ. This gives a normalized radius $r^* = r/R$ for each

164   grid column. Averaging is then applied over grid points that fall into the same r^* bins.

165   This way, we avoid the blurring that would result from azimuthal averaging over r bins.

166   At a given time, $R(\varphi)$ is here identified based on a filtered version of the kinetic energy

167   field $E_w(\varphi, r) = 0.5w(\varphi, r)^2$ at $z = 15$ m. $R(\varphi)$ is taken as the maximum radius at which

168   $E_w(\varphi, r)$ exceeds a threshold value. This method takes advantage of the lifting that occurs

169   right in front of the cold pool and $r^* = 1$ thus lies slightly ahead of the cold-pool edge.

170   Figure 2 shows the obtained r^*-z distributions of water-vapor density ($\rho_v = q_v\rho$; gray

171   shading) for the same three time steps after 26, 62, and 98 min. Also shown are contours of

172   the three tracer mass density distributions due to latent-heat fluxes ($\rho'_{lh} = q'_{lh}\rho$; orange),

173   evaporation of rain ($\rho'_{er} = q'_{er}\rho$; blue), and the pre-rain PBL water-vapor perturbation

174   ($\rho'_{pbl} = q'_{pbl}\rho$; red). These are contoured every 0.2 kg^{-1} (line labels are multiplied by 10).

175   The average R is indicated on top of each panel.

176   During the early stage, at $t = 26$ min, the downdraft air undercuts the boundary-layer

177   air mass. The displaced air indeed carries the largest moisture content, but not – as pre-

178   viously argued by TO1 and others – due to evaporative moistening, but because the PBL

179   was relatively moist in the first place. The water-vapor mass from evaporation that is car-

180   ried by air between the leading edge and the center (~ 0.2 g kg^{-1}) is considerably smaller

181   than the pre-rain water-vapor perturbation carried in the leading edge (~ 1.2 g kg^{-1}).

182   The contribution from surface fluxes is also small at that time. It peaks near the surface

183   close to the leading edge.

184   Later, after 62 and 98 minutes, the perturbation is mostly made up by water-vapor mass

185   that was supplied by surface latent-heat fluxes. The latter cause a distinct perturbation

near the leading edge with considerable vertical extent. In line with laboratory flows

of density currents [e.g., *Simpson and Britter*, 1979], the near-surface flow inside the

cold pool is considerably faster (about twice; not shown) than the propagation speed

of the leading edge. This leads to the enhancement of surface fluxes as seen also in

previous studies [*Young et al.*, 1995; *Redelsperger et al.*, 2000; *Yokoi et al.*, 2014] and to

the transport towards and into the leading edge of the cold pool. At $t = 98$ min, the pre-

rain PBL moisture has been lofted off the ground and significantly dispersed with minor

contributions near the leading edge. The bulk of the evaporated rain mass trails behind

the leading edge of the cold pool with small contributions to the low-level perturbation

near $r^* = 1$. Note also that the vapor mass perturbation is clearly carried inside the cold

pool and not outside or ahead of the leading edge as argued by *Schlemmer and Hohenegger*

[2014] and *Li et al.* [2014].

4. PBL pre-moistening by evaporating rain?

Apparently, the evaporation of rain explains only a small fraction of the water-vapor

perturbation near the leading edge of cold pools. This is in sharp contrast to the prevailing

theory developed by TO1 which implies that the boundary-layer air gets moistened by the

evaporation of rain drops. A necessary condition for the validity of this theory is that there

is sufficient evaporation of rain drops before the original sub-cloud layer air gets replaced

by dry downdraft air from aloft. In other words, the time t_{req} required to moisten the

sub-cloud layer by about 0.7 g kg^{-1} (the magnitude of the vapor-ring anomaly; see Fig. 1)

has to be equal or smaller than the time t_{exp} during which the original sub-cloud layer air

206 is exposed to rain drops. The sub-cloud layer will get squashed outside of the rain shaft

207 by the approaching downdraft air. The latter thus sets t_{exp}.

It is demonstrated here that the ratio $t_{\text{req}}/t_{\text{exp}}$ is around three, even if an upper bound

on t_{exp} is considered. An upper bound on t_{exp} is obtained as the time it takes an air

parcel to sink from cloud base to the ground if it experiences only the minimal negative

buoyancy due to the weight of condensate. Additional factors – which decrease t_{exp} – such

as the additional acceleration due to evaporation of liquid water or an existing downdraft

at cloud base are neglected. Starting from a zero velocity at cloud base, the downdraft

velocity is assumed to evolve according to the plume model of *Simpson and Wiggert* [1969],

which has been applied previously to updrafts [*Jakob and Siebesma*, 2003; *Siebesma et al.*,

2003; *Gregory*, 2001] and downdrafts *Park* [2014], as

$$\frac{dw}{dt} = 0.5\frac{dw^2}{dz} = aB - b\epsilon w^2. \tag{7}$$

In line with our desire to obtain an upper bound on t_{exp}, this model accounts for the

adverse pressure gradient due to the arising inertial pressure and considers the drag due

to lateral mixing. Following *Gregory* [2001] and *Jakob and Siebesma* [2003], we use $a = 1/3$

and $b = 2$. A constant buoyancy B is assumed that results only from condensate loading

in the rain shaft below cloud base, such that $B = -gr_l/(1 + r_t)$ with g the gravitational

acceleration, r_l the rain mixing ratio, and $r_t = r_v + r_l$ the total water mixing ratio. The

analytical solution for $w(z)$ is given in the appendix. Given $w(z)$, the time t_{exp} it takes

to sink from $z = h$ to $z = 0$ is obtained by integrating $dt = w(z)^{-1}dz$, which gives

$$t_{\text{exp}} = \frac{1}{\sqrt{-ab\epsilon B}} \ln\left(\sqrt{e^{2b\epsilon h} - 1} + e^{b\epsilon h}\right). \tag{8}$$

For a cloud base at $h = 500$ m and a typical value of the fractional entrainment rate $\epsilon = 0.5 \cdot 10^{-3}$ m^{-1}, one yields exposure times $t_{\text{exp}} = [346, 300, 268]$ s for the simulated range in rain mixing ratios of $r_l = [3, 4, 5]$ g kg^{-1}.

The required time t_{req} is given as $t_{\text{req}} = \delta r_v / \overline{E}$ with δr_v the simulated vapor-ring perturbation of 0.7 g kg^{-1} (see Fig. 1) and $\overline{E}$ an average evaporation rate in the sub-cloud layer. The latter is $0.8 \cdot 10^{-6}$ s^{-1} in R1, yielding $t_{\text{req}} = 875$ s. Thus, $t_{\text{req}}/t_{\text{exp}}$ ranges between 2.5 and 3.3 for the specified range of rain mixing ratios. This simple estimate shows that – at best – only about one third of the anticipated δr_v can result from the evaporation of rain below cloud base. These numbers agree fairly well with our reference simulation which showed an evaporative water-vapor source of about 0.2 g kg^{-1} before air gets displaced laterally by the downdraft. Note also that a sensitivity experiment in which the evaporation of rain had been switched off resulted in the same dynamics in the sub-cloud layer during this initial stage of rainfall onset. Thus, the acceleration that squashes the sub-cloud air aside is indeed maintained by condensate loading rather than by the evaporation of rain drops.

5. Sensitivity to initial PBL moisture

The evaporation rate E of rain drops in the sub-cloud layer is largely controlled by relative humidity. Then, what if moist convection forms from a drier sub-cloud layer? Will the source from rain-drop evaporation increase due to larger evaporation rates?

To test this, we analyze simulation R2 and again decompose the water-vapor perturbation in the lowest 100 m into its different origins. The results are shown for two time steps (26 and 98 min) in Fig. 3. Even though this simulation is initialized without a PBL

229   moisture anomaly, surface latent-heat fluxes during the convergent period of convective

230   growth form a pre-rain moisture anomaly below the cloud. This surface-flux contribution

231   to the pre-rain anomaly is even larger than in R1, simply because the surface latent-heat

232   fluxes scale with the moisture gradient at the surface and R2 is drier than R1 (see section

233   2.1). For this reason, the pre-rain sub-cloud layer in R2 is not as dry as would be expected

234   in the absence of this feedback. On top of that, rain mixing ratios r_l in the rain shaft are

235   smaller than in R1 (not shown). This weakening of convective precipitation for a drier

236   initial boundary layer is in line with findings presented by *Droegemeier and Wilhelmson*

237   [1985] (their section 5b). Overall, the increase of E due to a smaller r_v is even overcom-

238   pensated by the decrease due to smaller r_l. The ratio of t_{req}/t_{exp} in R2 remains close to

239   the one in R1 as both t_{req} and t_{exp} increase. As a result, the evaporative contribution to

240   the water-vapor perturbation is again insignificant in R2 (see Fig. 3). As in R1, surface

241   latent-heat fluxes are the key player.

6. Conclusions

242   Rings of enhanced water-vapor concentrations are associated with the leading edges of

243   cold pools over tropical oceans. The idealized simulations of single cold pools carried out

244   in this letter replicate this observation for an atmosphere initialized with thermodynamic

245   profiles from radiative-convective equilibrium. In contrast to the prevailing theory, the

246   findings presented herein show that surface latent-heat fluxes are the primary cause for

247   such ring-shaped water-vapor anomalies. The evaporation of rain drops below cloud base

248   is found to be secondary since the sub-cloud layer is not exposed long enough to the rain

249   shaft before it gets displaced by the approaching dry downdraft air. The sub-cloud air

which gets displaced by the downdraft is indeed relatively moist, but not – as previously

believed – due to rain-drop evaporation, but simply because deep convection grows from

a relatively moist sub-cloud layer in the first place. Figure 4 summarizes the processes

relevant during different stages of the cold pool's life cycle.

To advance the parameterization of cold-pool effects on deep convection in GCMs, it

thus appears key to represent the effects of surface latent-heat fluxes within conceptual

models for subgrid-scale convection. Based on our results, a parameterization should

account for the enhanced latent-heat fluxes into the cold pool and the subsequent mass

transport into the cold-pool edges. Future research needs to establish a conceptual model

for the evolution of the magnitude of these water-vapor rings. On top of that, the effects

of enhanced water-vapor content on, e.g., convective inhibition, need to be considered to

account for the modified lifting trajectories of such thermodynamically conditioned air

parcels.

Appendix A: Analytical solution for $w(z)$

For constant b, ϵ, a, and B the analytical solution to equation (7) is

$$w(z) = w(z_0) - \sqrt{-\frac{aB}{b\epsilon}}\sqrt{1 - e^{-2b\epsilon(z_0 - z)}}, \qquad (A1)$$

with $0 \leq z \leq z_0$ and $B \leq 0$.

References

Addis, R. P., M. Grstang, and G. D. Emmitt (1984), Downdrafts from tropical oceanic cumuli, *Bound. Layer. Meteorol.*, *28*, 23–49.

Boing, S. J., H. J. J. Jonker, A. P. Siebesma, and W. W. Grabowski (2012), Influence of the Subcloud Layer on the Development of a Deep Convective Ensemble, *J. Atmos. Sci.*, *69*, 2682–2698.

Droegemeier, K. K., and R. B. Wilhelmson (1985), Three-dimensional numerical modeling of convection produced by interacting thunderstorm outflows. part I: Control simulation and low-level moisture variations, *J. Atmos. Sci.*, *42*, 2381–2403.

Grandpeix, J.-Y., and J.-P. Lafore (2010), A density current parameterization coupled with emanuels convection scheme. Part I: The models, *J. Atmos. Sci.*, *67*, 881–897.

Gregory, D. (2001), Estimation of entrainment rate in simple models of convective clouds, *Quart. J. Roy. Meteor. Soc.*, *127*, 53–72.

Jakob, C., and A. P. Siebesma (2003), A new subcloud model for mass-flux convection schemes: Influence on triggering, updraft properties, and model climate, *Mon. Wea. Rev.*, *131*, 2765–2778.

Khairoutdinov, M. F., S. K. Krueger, C.-H. Moeng, P. A. Bogenschutz, and D. A. Randall (2009), Large-eddy simulation of maritime deep tropical convection, *J. Adv. Model. Earth Syst.*, *1*, 13, doi:10.3894/JAMES.2009.1.15.

Kingsmill, D. E., and R. A. Houze (1999), Thermodynamic characteristics of air flowing into and out of precipitating convection over the west pacific warm pool, *Quart. J. Roy. Meteor. Soc.*, *125*, 1209–1229.

Klemp, J. B., W. C. Skamarock, and J. Dudhia (2007), Conservative split-explicit time integration methods for the compressible nonhydrostatic equations, *Mon. Wea. Rev.*, *135*, 2897–2913.

Krueger, S. K., Q. A. Fu, K. N. Liou, and H. N. S. Chin (1995), Improvements of an ice-phase microphysics parameterization for use in numerical simulations of tropical convection, *J. Appl. Meteorol.*, *34*, 281–287.

Langhans, W., K. Yeo, and D. M. Romps (2015), Lagrangian investigation of the precipitation efficiency of convective clouds, *J. Atmos. Sci.*, *72*, 1045–1062.

Li, Z., P. Zuidema, and P. Zhu (2014), Simulated convective invigoration processes at trade wind cumulus cold pool boundaries, *J. Atmos. Sci.*, *71*, 2823–2841; Corrigendum, *71*, 4710.

Lin, Y.-L., D. F. Richard, and H. D. Orville (1983), Bulk parametrization of the snow field in a cloud model, *J. Appl. Meteor.*, *22*, 1065–1092.

Lord, S. J., H. E. Willoughby, and J. M. Piotrowicz (1984), Role of a parameterized ice-phase microphysics in an axisymmetric, nonhydrostatic tropical cyclone model, *J. Atmos. Sci.*, *41*, 2836–2848.

Margolin, L. G., W. J. Rider, and F. F. Grinstein (2006), Modeling turbulent flow with implicit LES, *J. Turbul.*, *7*, 1–27.

Moeng, C.-H., and A. Arakawa (2012), Representation of boundary layer moisture transport in cloud-resolving models, *Mon. Wea. Rev.*, *140*, 3682–3698.

Moeng, C.-H., M. A. LeMone, M. F. Khairoutdinov, S. K. Krueger, P. A. Bogenschutz, and D. A. Randall (2009), The tropical marine boundary layer under a deep convection system: a large-eddy simulation study, *J. Adv. Model. Earth Syst.*, *1*, 13, doi: 10.3894/JAMES.2009.1.15.

Moncrieff, M. W., and C. Liu (1999), Convection initiation by density currents: Role of convergence, shear, and dynamical organization, *Mon. Wea. Rev.*, *127*, 2455–2464.

Park, S. (2014), A Unified Convection Scheme (UNICON). Part I: Formulation, *J. Atmos. Sci.*, *71*, 3902–3930.

Qian, L., G. S. Young, and W. M. Frank (1998), A convective wake parameterization scheme for use in general circulation models, *Mon. Wea. Rev.*, *126*, 456–469.

Redelsperger, J., F. Guichard, and S. Mondon (2000), A parameterization of mesoscale enhancement of surface fluxes for large-scale models, *J. Climate*, *13*, 402–421.

Rio, C., et al. (2013), Control of deep convection by sub-cloud lifting processes: the ALP closure in the LMDZ5B general circulation model, *Clim. Dyn.*, *40*, 2271–2292.

Romps, D. M. (2008), The Dry-Entropy Budget of a Moist Atmosphere, *J. Atmos. Sci.*, *65*, 3779–3799.

Romps, D. M., and Z. Kuang (2011), A Transilient Matrix for Moist Convection, *J. Atmos. Sci.*, *68*, 2009–2025.

Rotunno, R., J. B. Klemp, and M. L. Weisman (1988), A theory for strong, long-lived squall lines, *J. Atmos. Sci.*, *45*, 463–485.

Schlemmer, L., and C. Hohenegger (2014), The formation of wider and deeper clouds as a result of cold-pool dynamics, *J. Atmos. Sci.*, *71*, 2842–2858.

Seifert, A., and T. Heus (2013), Large-eddy simulation of organized precipitating trade wind cumulus clouds, *Atmos. Chem. Phys.*, *13*, 5631–5645.

Shu, C. W., and S. Osher (1988), Efficient implementation of essentially non-oscillatory shock-capturing schemes, *J. Comput. Phys.*, *77*, 439–471.

Siebesma, A. P., C. S. Bretherton, A. Brown, et al. (2003), A large eddy simulation intercomparison study of shallow cumulus convection, *J. Atmos. Sci.*, *60*, 1201–1219.

Simpson, J., and V. Wiggert (1969), Models of precipitating cumulus towers, *Mon. Wea. Rev.*, *97*, 471–489.

Simpson, J. E., and R. E. Britter (1979), The dynamics of the head of a gravity current advancing over a horizontal surface, *J. Fluid Mech.*, *94*, 477–495.

Thuburn, J. (1996), Multidimensional flux-limited advection schemes, *J. Comput. Phys.*, *123*, 74–83.

Tompkins, A. M. (2001a), Organization of tropical convection in low vertical wind shears: The role of water vapor, *J. Atmos. Sci.*, *58*, 529–545.

353 Tompkins, A. M. (2001b), Organization of tropical convection in low vertical wind shears:

354   The role of cold pools, *J. Atmos. Sci.*, *58*, 1650–1672.

355 Torri, J., Z. Kuang, and Y. Tian (2015), Mechanisms for convection triggering by cold

356   pools, *Geophys. Res. Let.*, doi:10.1002/2015GL063227, in press.

357 Xue, H., G. Feingold, and B. Stevens (2008), Aerosol effects on clouds, precipitation, and

358   the organization of shallow cumulus convection, *J. Atmos. Sci.*, *65*, 392–406.

359 Yokoi, S., M. Katsumata, and K. Yoneyama (2014), Variability in surface meteorology and

360   air-sea fluxes due to cumulus convective systems observed during CINDY/DYNAMO,

361   *J. Geophys. Res.*, *119*, 2064–2078.

362 Young, G. S., S. M. Perugini, and C. W. Fairall (1995), Convective wakes in the equatorial

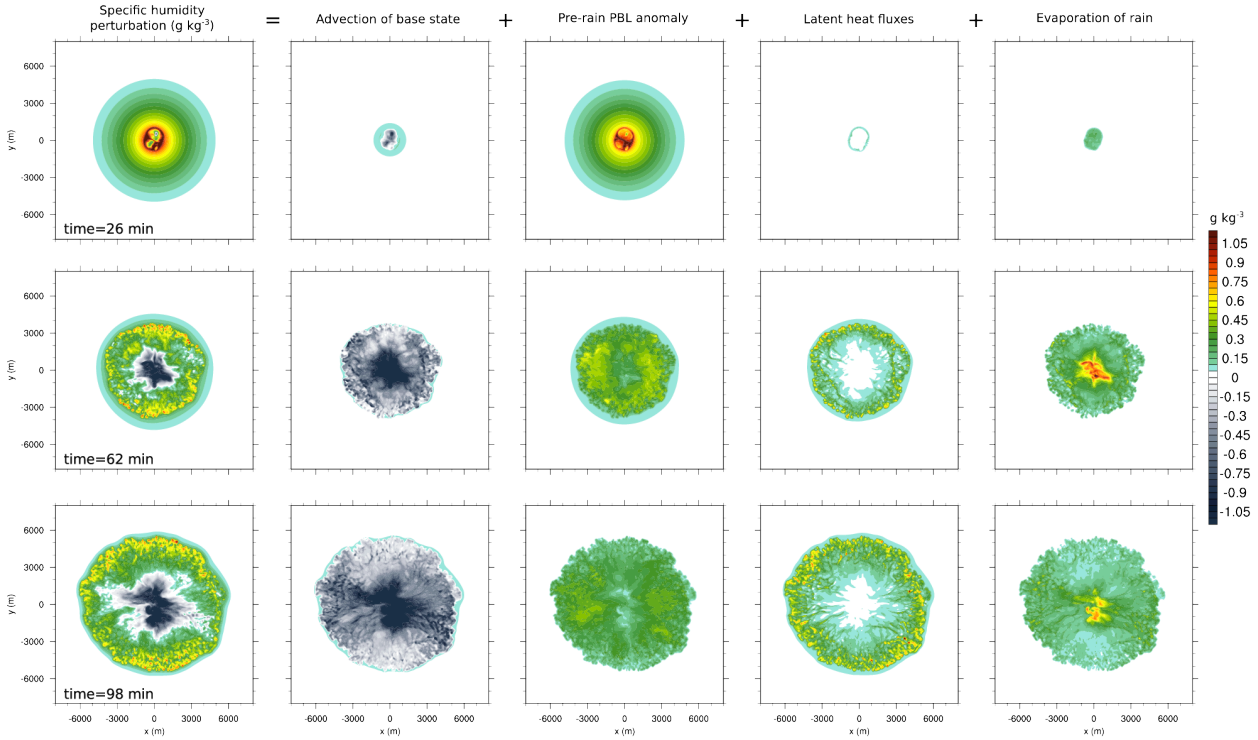363   western Pacific during TOGA, *Mon. Wea. Rev.*, *123*, 110–123.

Figure 1. Decomposition of the (1st column) perturbation water-vapor mass fraction q_v' into contributions from (2nd column) the advection of the base-state perturbation q_{base}', (3rd column) the advection of the pre-rain PBL anomaly q_{pbl}', (4th column) latent-heat fluxes q_{lh}', and (5th column) evaporation of rain q_{er}'. Distributions are from simulation R1 and shown after 26, 62, and 98 min. All quantities are computed as density-weighted vapor-mass fractions for the lowest 100 meters (see Eq. (6)). To obtain the perturbations in column 1 and 2, the far-field value of the base-state vapor mass fraction has been subtracted from the actual vapor mass fraction (1st column) and from the base-state mass fraction (2nd column). To very good approximation, the sum of the four rightmost panels yields the leftmost panel.
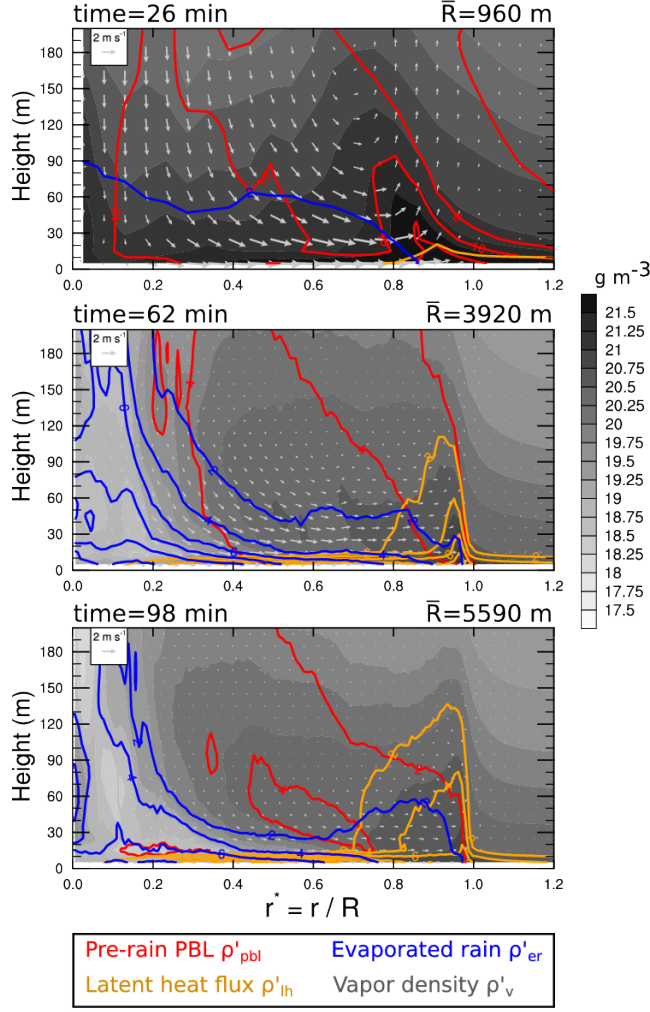
Figure 2. Azimuthally averaged r^*-z distributions of the water-vapor density ρ_v (g m^{-3}; gray shading) and of the individual perturbations due to latent-heat fluxes ρ'_{lh} (orange contours), due to evaporation of rain ρ'_{er} (blue contours), and due to the pre-rain PBL anomaly ρ'_{pbl} (red contours) are shown for simulation R1 after 26, 62, and 98 min. The three perturbations are contoured every 0.2 g m^{-3} starting at 0.2 g m^{-3} (line labels are multiplied by 10). Vectors illustrate the average velocity field. A normalized radial distance $r^* = r/R$ has been computed first for each grid column with R the radius at the leading edge of the cold pool determined as described in the text. Averaging is then performed over r^* bins of width $dr^* = 50\text{m}/\overline{R}$ with $\overline{R}$ the average R, which is indicated on top of each panel.
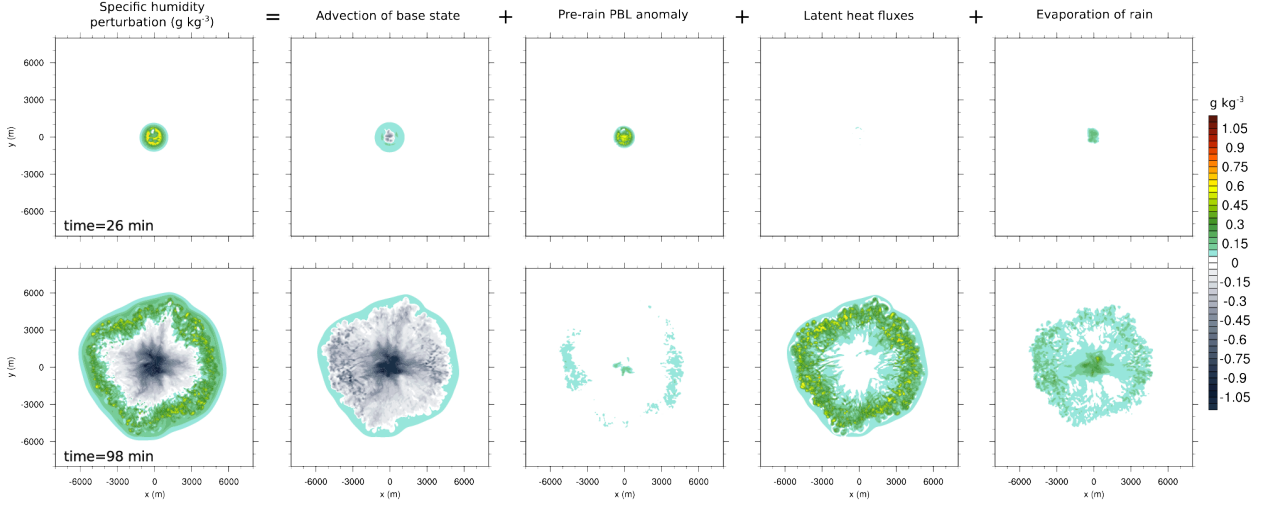
Figure 3.   Same as Fig. 1, but for simulation R2, which is initialized without a moisture perturbation. Only two time steps are shown. The pre-rain PBL water-vapor perturbation visible here is only caused by surface latent-heat fluxes during the period of convergent near-surface flow.
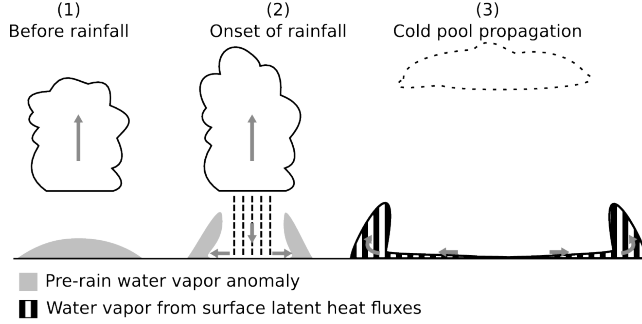
Figure 4.   Schematic of the processes responsible for water-vapor rings in tropical cold pools. (1) A water-vapor perturbation exists below cloud base before rainfall sets in. Deep convective clouds rise from sub-cloud layers that are relatively moist due to, e.g., the vapor ring of an older cold pool. Even without a pre-existing vapor ring, the pre-rain moisture excess below cloud base can result solely from enhanced surface fluxes during the early convergent period of cumulus growth. (2) The weight of rain drops is sufficient to maintain a downdraft that displaces the sub-cloud layer out of the rain shaft such that the exposure time of the sub-cloud layer to rain evaporation is short. The displaced and undercut air mass is relatively moist primarily due to the pre-rain water-vapor anomaly; the source from rain evaporation remains secondary. (3) The cold cool spreads radially and surface latent-heat fluxes continuously supply water-vapor mass that gets fluxed towards and into the leading edge of the cold pool.